

Article

Hollow TiO₂ Microsphere/Graphene Composite Photocatalyst for CO₂ Photoreduction

Yi-Chen Chung [†] , Pei-Jie Xie [†], Yi-Wei Lai and An-Ya Lo ^{*†} 

Department of Chemical and Materials Engineering, National Chin-Yi University of Technology, Taichung 411030, Taiwan; zxczaxzsbnm@gmail.com (Y.-C.C.); 3a518131@gm.student.ncut.edu.tw (P.-J.X.); 4A714012@gm.student.ncut.edu.tw (Y.-W.L.)

* Correspondence: a.y.lo1125@gmail.com or aylo@ncut.edu.tw

† Both authors contributed equally to this work.

Abstract: In an attempt to improve the photocatalytic activity of anatase TiO₂, we developed a composite photocatalyst composed of hollow TiO₂ microspheres (hTS) and graphene. The hTS were prepared through a two-step hydrothermal process, where SiO₂ microspheres with desirable diameters of 100–400 nm were used as sacrificial templates. Accordingly, the effect of the hTS cavity size on the activity of the catalyst in wet CO₂ photoreduction (CO₂PR) was studied. Furthermore, it was established that the hydrothermal pH value crucially influences the photocatalytic activity of the hTS photocatalyst, as well as its composition and microstructure. The hTS photocatalyst was also combined with graphene (0–90 wt%) to improve its photocatalytic activity. This study provides insight into the optimal microsphere diameter, hydrothermal pH value, and graphene/hTS_x ratio required for designing hollow microsphere-based photocatalysts with enhanced CO₂PR performances.

Keywords: CO₂ photoreduction; graphene; TiO₂; hollow microspheres



Citation: Chung, Y.-C.; Xie, P.-J.; Lai, Y.-W.; Lo, A.-Y. Hollow TiO₂ Microsphere/Graphene Composite Photocatalyst for CO₂ Photoreduction. *Catalysts* **2021**, *11*, 1532. <https://doi.org/10.3390/catal11121532>

Academic Editor: Omid Akhavan

Received: 9 November 2021

Accepted: 11 December 2021

Published: 16 December 2021

Publisher's Note: MDPI stays neutral with regard to jurisdictional claims in published maps and institutional affiliations.



Copyright: © 2021 by the authors. Licensee MDPI, Basel, Switzerland. This article is an open access article distributed under the terms and conditions of the Creative Commons Attribution (CC BY) license (<https://creativecommons.org/licenses/by/4.0/>).

1. Introduction

Scientists and engineers have been developing diverse green technologies, ranging from CO₂ capture to renewable energy and energy conversion devices, to combat the ever-increasing impact of the greenhouse effect and energy crisis on the environment [1–8]. CO₂ photoreduction (CO₂PR) is the only technology that can consume CO₂ to produce valuable fuels using solar energy. Since the 1990s, research interest in CO₂PR has grown exponentially owing to the rapid development of semiconductor photocatalysts [9].

Anatase TiO₂ is the most widely adopted semiconductor material for CO₂PR owing to its excellent stability, nontoxicity, and low cost [10,11]. However, its performance is limited by its large bandgap of approximately 3.2 eV [12,13]. Strategies to improve the photocatalytic performance of anatase TiO₂ commonly involve incorporating it into various materials or implementing nanoporosity [5,12,14,15]. Some of these methods include heteroatom doping [15–17], quantum dot decoration [18], additional semiconductor hybridization [19], and dye sensitization [20]. As these methods combine photocatalysts with sophisticated materials, coupling them with a simpler material, such as graphene, is a more straightforward approach. Graphene is an effective catalyst support that can improve the CO₂PR performance of a catalyst by accelerating electron–hole separation, enhancing CO₂ adsorption through π – π conjugation, improving the catalyst specific surface area (SSA), enhancing the catalyst light utilization, and activating CO₂ molecules [21,22]. Mesoporous and microporous materials have also been widely studied as photocatalysts for CO₂PR owing to their high SSAs and ability to rapidly diffuse reactants/products; however, they have relatively slow convection rates, which limits their overall mass transfer of reactants/products [12,15]. Therefore, developing a photocatalyst with an optimal-sized macroporous structure could elucidate the effect of the photocatalyst pore size on CO₂PR.

In this study, we present a simple approach for the preparation of a photocatalyst for gas-phase wet CO₂PR. The photocatalyst comprises hollow TiO₂ microspheres that are coupled with graphene (0–90 wt%; denoted as hTS_{x-y}G_z, where subscript x, y, and z represent the average diameter, processing pH value, and graphene mass fraction, respectively) to effectively improve the photocatalytic activity of the TiO₂ microspheres. Notably, the hTS used in this study possess desirable diameters of 100–400 nm, and an optimal graphene/hTS_x ratio was achieved. This protocol also serves as a guideline for the design of hollow microsphere-based photocatalysts for CO₂PR.

2. Results and Discussion

2.1. Structure and Crystalline Properties

The surface morphologies of the silica microspheres (SS_x, where x refers to the average diameter), with average particle sizes of 100, 200, 300, and 400 nm (designated as SS₁₀₀, SS₂₀₀, SS₃₀₀, and SS₄₀₀, respectively), were analyzed via scanning electron microscopy (SEM; Figure 1a–d); the processing parameters and diameter ranges are listed in Table S1. A hydrothermal process was then used to apply a TiO₂-shell over each SS_x core, using titanium (IV) butoxide (TBT) as the TiO₂ precursor, to give the corresponding core-shell SiO₂-TiO₂ microspheres (TS_x). The surface morphologies of TS₁₀₀, TS₂₀₀, TS₃₀₀, and TS₄₀₀ were also examined via SEM (Figure 1e–h), revealing rougher surfaces than those of their corresponding SS₁₀₀, SS₂₀₀, SS₃₀₀, and SS₄₀₀ cores. In addition, it is clear that the particle sizes increased by 20–60 nm upon addition of the TiO₂-shells, indicating that the thicknesses of the shells are approximately 10–30 nm. X-ray diffraction (XRD) analyses also confirmed the successful coating of the SS_x with the desired TiO₂ species. Specifically, comparing the XRD patterns of the SS_x and TS_x (Figure S1a,b, respectively) verified the presence of weak but characteristic anatase peaks in the latter.

The pH values of the catalyst solutions were adjusted to 8, 10, 12, or 14 for the subsequent hydrothermal process applied to remove the SiO₂ core, followed by calcination at 470 °C. The SEM images of the resultant hollow TiO₂ microsphere (hTS_{x-y} in which y refers to the pH; hTS₂₀₀₋₈, hTS₂₀₀₋₁₀, hTS₂₀₀₋₁₂, and hTS₂₀₀₋₁₄) photocatalyst surfaces are shown in Figure 2a–d, and the mass fraction of residual SiO₂ in each sample is provided in Table S2. At pH 8 and 10, the sodium hydroxide concentration was too low to remove the SiO₂ core from the TiO₂ shell. As a result, there are large amounts of residual SiO₂ in hTS₂₀₀₋₈ (65 wt%) and hTS₂₀₀₋₁₀ (51 wt%), as indicated in the scanning electron microscopy-energy dispersive spectroscopy (EDS) results. With an increase in the pH to 12, the morphology of the TiO₂ shell became nanoflake-like (Figure 2c), which greatly improved the SSA (141.88 m²/g) of the photocatalyst. As a result, the majority of the SiO₂ core was removed (4.1 wt% residual SiO₂) while maintaining the hierarchical structure of the microsphere. At a hydrothermal pH ≤ 12, the EDS and Fourier-transform infrared (FTIR) (Figure S2) analyses showed similar results regarding the effect of the processing pH on the hTS_{x-y} structures; however, a further increase in the pH to 14 destroys the microspheres. The hollow microsphere structure of hTS_{x-y} was clearly observed via transmission electron microscopy (TEM) (Figure S3), indicating that our proposed two-step hydrothermal method can effectively remove the SiO₂ core and produce the desired TiO₂ shell, resulting in the target hollow microspheres.

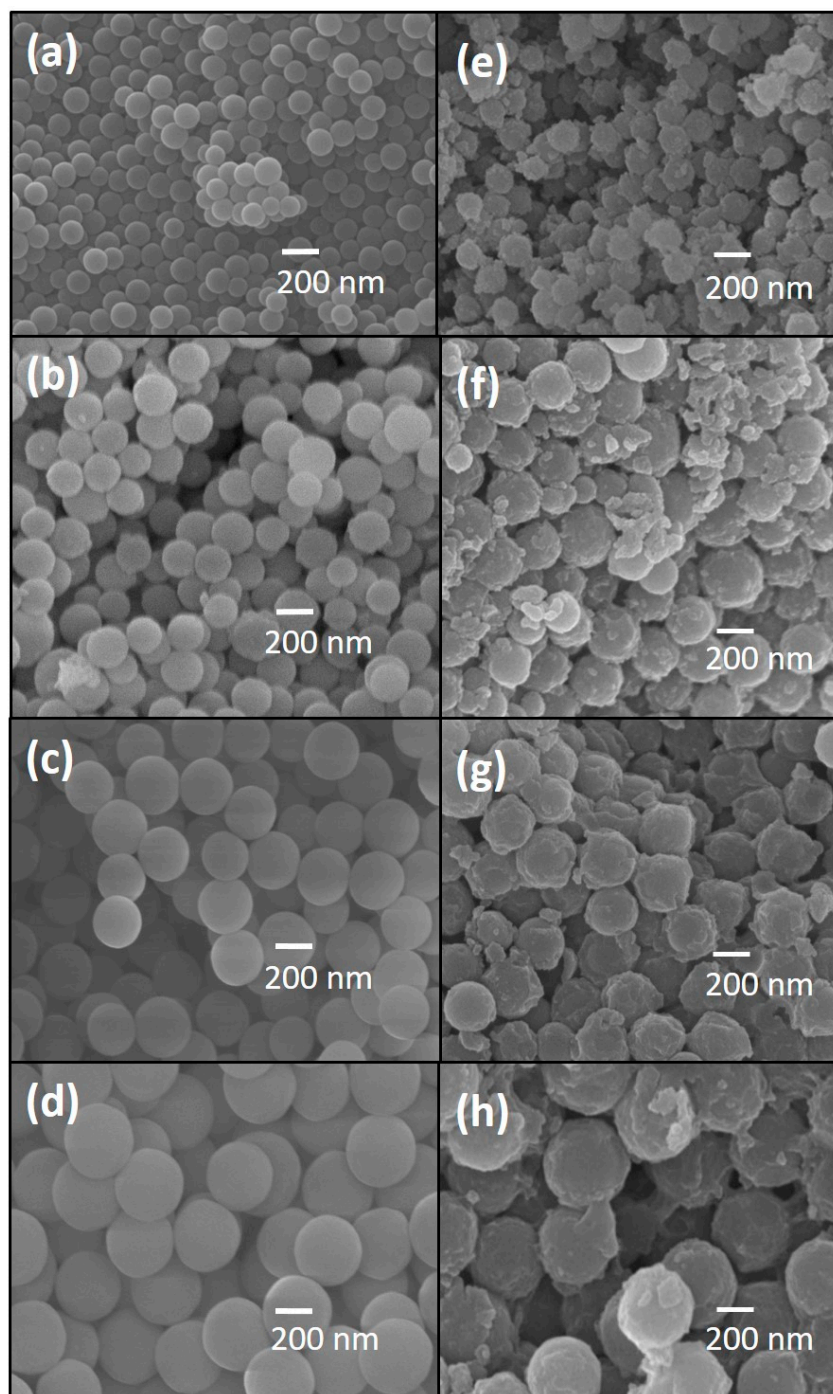


Figure 1. Scanning electron microscopy (SEM) images of the silica microspheres (SS_x ; x = average diameter) and those of the corresponding TiO_2 -coated microspheres (TS_x): (a) SS_{100} , (b) SS_{200} , (c) SS_{300} , (d) SS_{400} , (e) TS_{100} , (f) TS_{200} , (g) TS_{300} , and (h) TS_{400} .

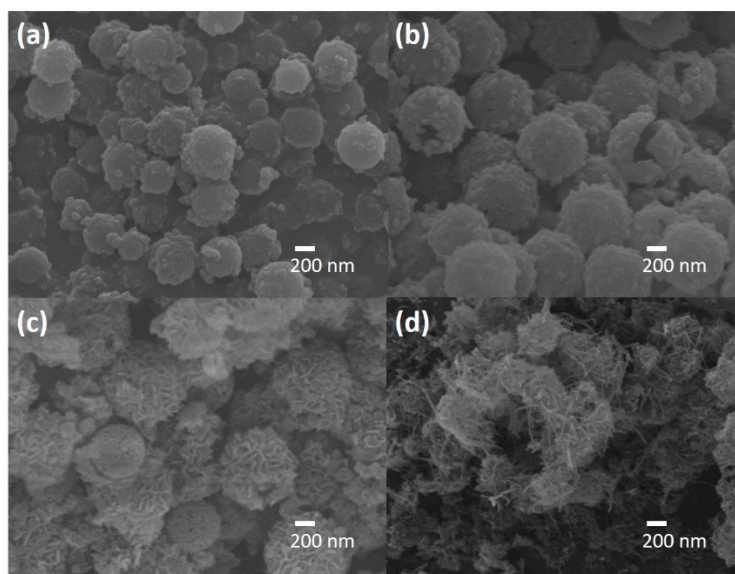


Figure 2. SEM images of the prepared hollow TiO₂ microspheres (hTS_{x-y}; x = average diameter, y = pH used during the hydrothermal process): (a) hTS₂₀₀₋₈, (b) hTS₂₀₀₋₁₀, (c) hTS₂₀₀₋₁₂, and (d) hTS₂₀₀₋₁₄.

The XRD patterns of hTS₂₀₀₋₈, hTS₂₀₀₋₁₀, hTS₂₀₀₋₁₂, and hTS₂₀₀₋₁₄ (Figure 3) only show characteristic TiO₂ diffraction peaks when a hydrothermal pH of at least 12 is used. Specifically, the XRD pattern of hTS₂₀₀₋₁₂ exhibits diffraction peaks corresponding to the (101), (103), (004), (112), (200), (105), (211), and (204) planes of anatase TiO₂ (JCPDS no. 00-021-1272). However, an increase in the pH to 14 (i.e., hTS₂₀₀₋₁₄) slightly shifts the peaks to lower two theta values, resulting in a pattern that better resembles that of the anatase phase. This indicates the presence of lattice strain in hTS₂₀₀₋₁₂, which is likely owing to stress induced by its lattice defects; although such defects have reportedly resulted in improved photocatalytic activity [23]. In contrast, 77 K N₂ adsorption/desorption evaluations indicated that the SSAs of the resultant photocatalysts follow the order: hTS₂₀₀₋₁₂ (141.88 m²/g) >> hTS₂₀₀₋₁₄ (64.93 m²/g) > hTS₂₀₀₋₁₀ (41.64 m²/g) > hTS₂₀₀₋₈ (37.92 m²/g). The low SSAs of hTS₂₀₀₋₁₀ and hTS₂₀₀₋₈ are attributed to the large amounts of residual SiO₂ present in the materials; this is supported by the larger SSA of hTS₂₀₀₋₁₂, as it contained less residual SiO₂ than hTS₂₀₀₋₁₀ and hTS₂₀₀₋₈. The maximum SSA was observed for hTS₂₀₀₋₁₂, as increasing the processing pH to 14 leads to the collapse of the microsphere and thus a reduced SSA. Therefore, the characterization results suggest that among these four samples, hTS₂₀₀₋₁₂ would perform best as a photocatalyst.

2.2. Photocatalytic CO and CH₄ Production

2.2.1. Effect of the Processing pH of the Catalyst on Its Photocatalytic Performance

The UV-vis diffuse reflectance spectroscopy (UV-DRS) spectra of the hTS_{200-y} samples (Figure 4) show that the absorption edges continuously red-shift with a gradual increase in the processing pH of the catalysts; this implies a narrowing of their band gaps. Further analysis using Tauc plots indicated that the band gaps followed the order: hTS₂₀₀₋₁₂ (3.4 eV) < hTS₂₀₀₋₁₄ (3.6 eV) < hTS₂₀₀₋₈ (3.9 eV) = hTS₂₀₀₋₁₀ (3.9 eV). Therefore, the large band gaps of the samples processed at pH 8 and 10 can be attributed to the large amounts of residual SiO₂ they contain (hTS₂₀₀₋₈, 65 wt%; hTS₂₀₀₋₁₀, 51 wt%). However, only 4.1 wt% SiO₂ remained in the sample prepared at a pH of 12 (hTS₂₀₀₋₁₂). This Si impurity induced the lattice strain observed in the XRD pattern of hTS₂₀₀₋₁₂ (as discussed in Section 3.1) and resulted in this catalyst exhibiting the smallest band gap. A further increase in the pH to 14 led to enhanced anatase TiO₂ crystallization (as discussed in Section 3.1), and, thus, an increase in the hTS₂₀₀₋₁₄ band gap.

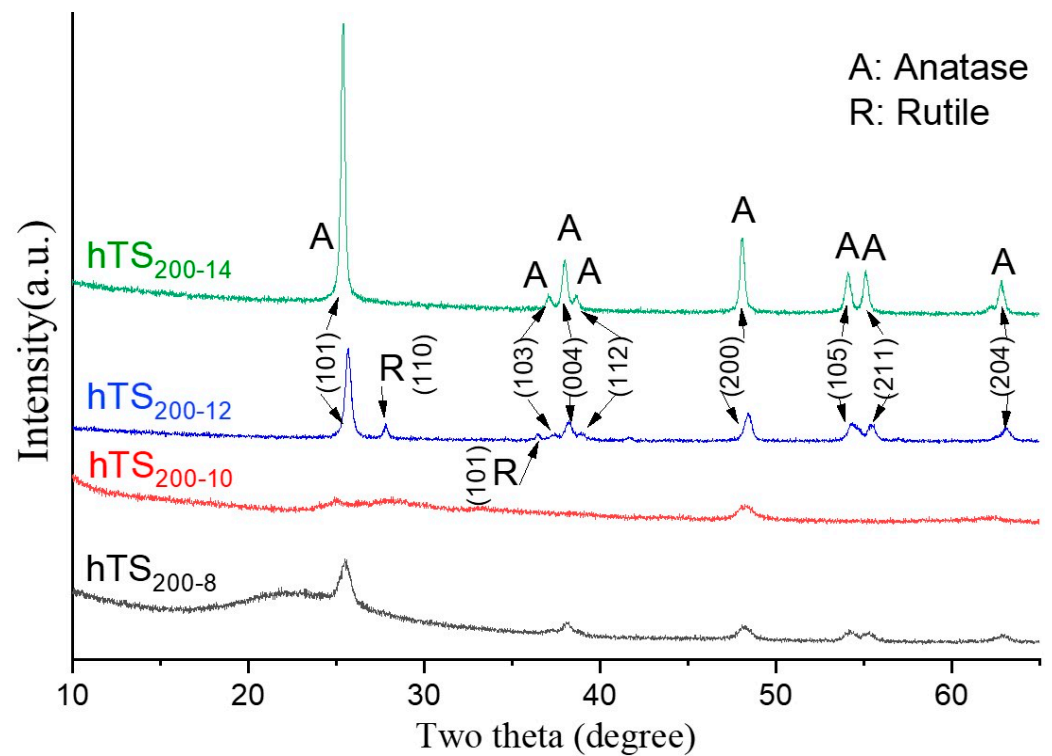


Figure 3. X-ray diffraction (XRD) patterns of the hTS_{200-8} , hTS_{200-10} , hTS_{200-12} , and hTS_{200-14} samples.

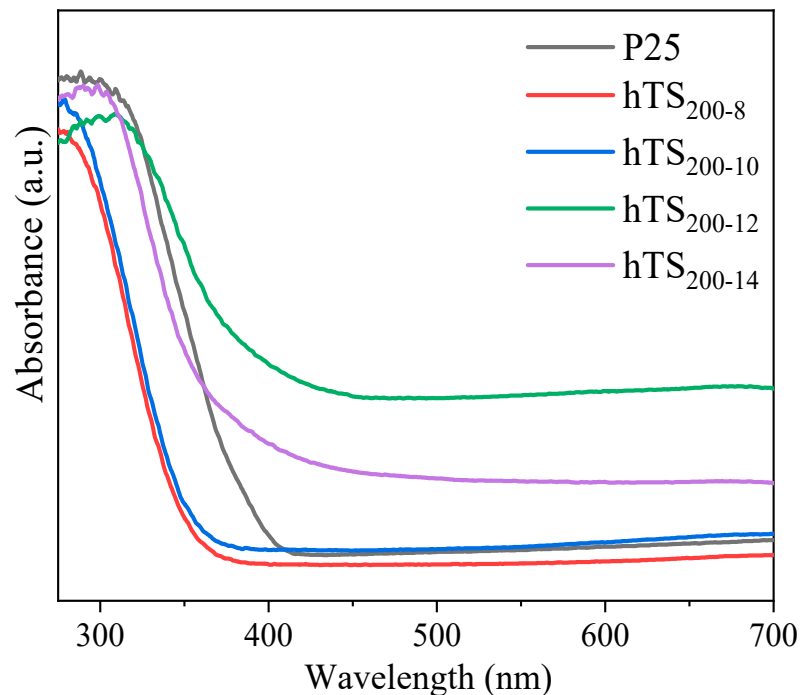


Figure 4. UV-vis diffuse reflectance spectroscopy (UV-DRS) spectra of the hTS_{200-y} photocatalysts.

The effects of the hydrothermal pH on the actual performance of the hTS_{200-8} , hTS_{200-10} , hTS_{200-12} , and hTS_{200-14} photocatalysts in CO_2 PR were subsequently examined (Figure 5). Both the CO and CH_4 production rates increase with an increase in the processing pH up to a pH > 12. Owing to their poor anatase crystallinities (Figure 3), hTS_{200-8} and hTS_{200-10} exhibit much poorer overall performances than the other photocatalysts. Although hTS_{200-14} exhibits the highest level of crystallinity, its inferior band gap and SSA to those of hTS_{200-12}

result in its CO and CH₄ production efficiencies being lower than those of hTS₂₀₀₋₁₂. The CO and CH₄ production efficiencies of the photocatalysts follow the order: hTS₂₀₀₋₁₂ >> hTS₂₀₀₋₁₄ >> hTS₂₀₀₋₈ > hTS₂₀₀₋₁₀, which coincides with the variations in their band gaps and SSAs (Table S2).

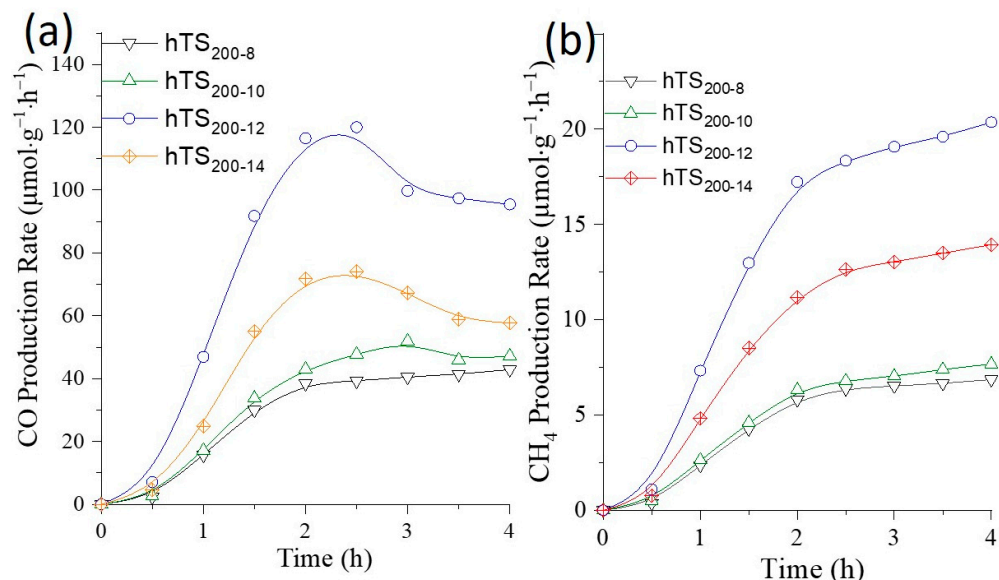


Figure 5. CO₂ photoreduction (CO₂PR) performance of the hTS_{200-y} photocatalysts as a function of the processing pH of the catalysts: (a) CO, and (b) CH₄ yields.

2.2.2. Effect of the Catalyst Cavity Size on Its Photocatalytic Performance

Employing the optimal catalyst processing pH (12), the effect of the cavity sizes of the hTS₁₀₀₋₁₂, hTS₂₀₀₋₁₂, hTS₃₀₀₋₁₂, and hTS₄₀₀₋₁₂ photocatalysts (i.e., the macropore size) on their CO₂PR activity was evaluated in our homemade CO₂PR system. Figure 6 shows the CO and CH₄ production rates achieved during irradiation in the presence of the photocatalysts; CO is the major product. The CO/CH₄ production rates achieved by the hTS_{x-12} photocatalysts increase during the first 2 h, owing to irradiation-induced catalyst activation. Upon reaching their maximum values after approximately 2 h of irradiation, the CO production rates leveled off and those of CH₄ increased at a much slower rate; the CO and CH₄ production rates with hTS₂₀₀₋₁₂ and hTS₃₀₀₋₁₂, respectively, first achieved decrease before levelling off. The results in Figure 5 show a similar trend. After 4 h, the maximum CO yields obtained using commercial P25, hTS₁₀₀₋₁₂, hTS₂₀₀₋₁₂, hTS₃₀₀₋₁₂, and hTS₄₀₀₋₁₂ were 37.2, 60.1, 95.2, 89.7, and 77.4 µmole/g h, respectively. The hTS₂₀₀₋₁₂ sample achieved the highest CO production rate, which could be due to various factors, including its light utilization efficiency, SSA, mass transfer abilities, and catalyst utilization rate. For example, it is well known that the SSA of particles decrease with an increase in their size; in contrast, the convection and diffusion rates of products/reactants increase and decrease, respectively, with an increase in the particle size. Consequently, the optimized performance was achieved using microspheres with a diameter of 200 nm. Notably, all the hTS_{x-12} photocatalysts outperformed the commercial P25 nanoparticles, which emphasizes the advantages of applying hollow microspheres as photocatalysts for CO₂PR.

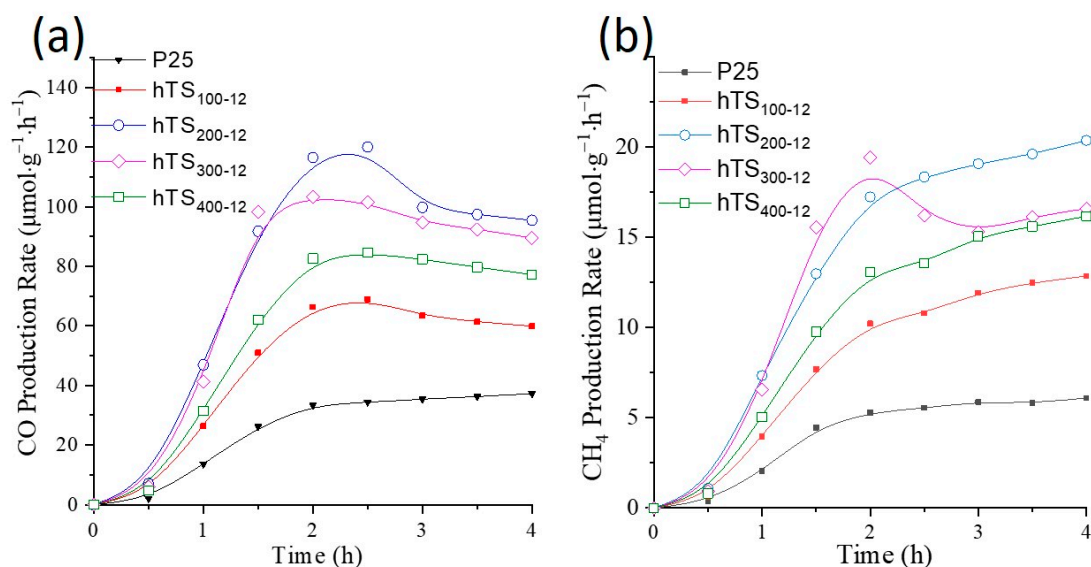


Figure 6. CO and CH₄ production via CO₂PR as a function of the hTS_{x-12} diameter: (a) CO, and (b) CH₄ yields.

Other than the cavity size, photogenerated electrons with higher reduction potentials offer overpotential for chemical reactions, e.g., the production of CO ($2e^-$, -0.53 V) and CH₄ ($8e^-$, -0.24 V). The reduction potential of a species is a measure of its ability to gain electrons. To reduce CO₂ into CO or CH₄, the electrons in the conducting band should have a more negative chemical potential than the reduction potentials [24]. From a thermodynamic perspective, the production of CH₄ is more favorable than that of CO, as CH₄ is produced at a lower potential. However, the kinetic limitation makes CH₄ production more difficult than CO production because more electrons are required for the production of CH₄ [25]. Moreover, the actual redox potential of the reaction is determined by the reaction pathway followed; a series of one-electron processes or a one-step multi-electron process can occur between the photocatalyst and absorbed CO₂. Therefore, an excited electron with a more negative reduction potential will result in the formation of multiple products during CO₂PR. Generally, the overall production rate is related to the active surface area of the catalyst and the selectivity of each product is related to complex surface properties, including excitation/recombination of electron-hole pairs and the charge transfer efficiency of the photocatalysts [26]. Over our proposed hTS_{x-12} photocatalysts, the production rates of CO and CH₄ show similar trends, suggesting that the product selectivity did not change over time; this has also been reported in the literature [27].

Considering the long-term stability, the hTS₂₀₀₋₁₂ photocatalyst with optimized hydrothermal pH value and cavity size was examined under irradiation for 24 h. As can be seen in Figure S4, there was no decay observed on CO and CH₄ production rates within 24 h, which shows computable stability among the TiO₂-based photocatalysts [28–30].

2.3. Effect of the hTS₂₀₀₋₁₂/Graphene Ratio on Its Photocatalytic Performance

To improve the dispersion of the photocatalysts and enhance their light utilization and photoactivity, hTS₂₀₀₋₁₂ was hybridized with 5, 30, 45, 50, 60, 70, 80, and 90 wt% graphene to produce hTS₂₀₀₋₁₂/graphene composites (hTS₂₀₀₋₁₂G_z; z = wt% graphene). The SEM images of the hybrids show that an increase in the amount of graphene from 5 to 50 wt% reduces the extent of hTS₂₀₀₋₁₂ agglomeration (Figure 7a–d). Further increasing the graphene mass fraction gradually increased the exposure of the surface of hTS₂₀₀₋₁₂G_z (Figure 7e–h). The CO/CH₄ production rates during irradiation in the presence of the composites were evaluated (Figure S5). Interestingly, at a graphene amount of ≤ 50 wt%, the rate–time curves between 0 and 2 h are concave upward with small initial slopes. This can be attributed to hTS₂₀₀₋₁₂ agglomeration, which leads to slow mass transfer of the reactants/products and inhibits activation of the photocatalyst. In contrast, the rate–

time curves obtained over the same time range when using the composites comprising >50 wt% graphene are concave downward with high initial slopes. This suggests that the incorporation of >50 wt% graphene improves the dispersity of hTS₂₀₀₋₁₂, allowing its efficient contact with the reaction gases; therefore, hTS₂₀₀₋₁₂ is activated and reaches its maximum activity more quickly when coupled with >50 wt% graphene.

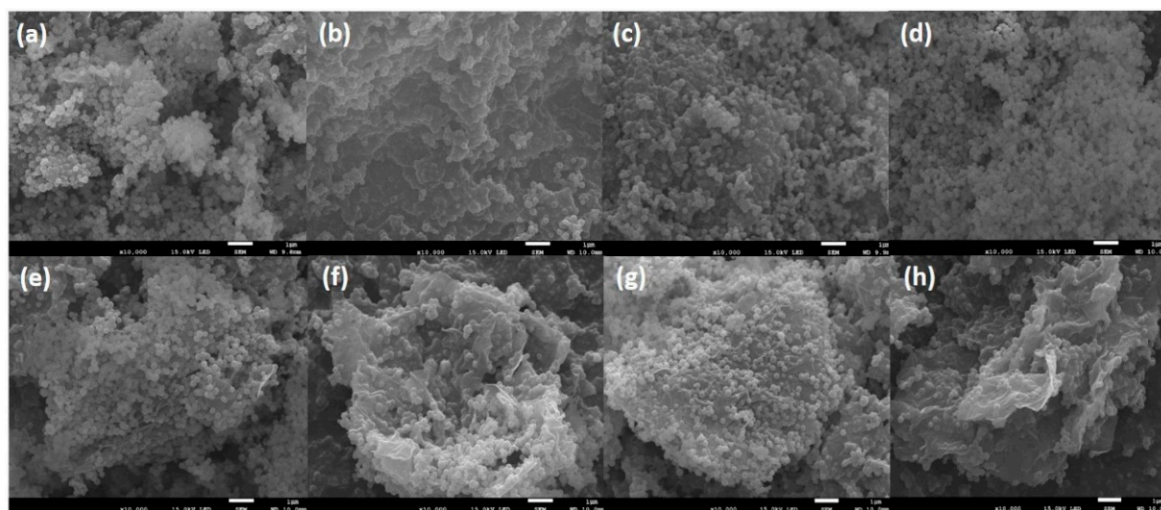


Figure 7. SEM images of the hTS₂₀₀₋₁₂/graphene composites (hTS₂₀₀₋₁₂G_z; z = wt% of graphene): hTS₂₀₀₋₁₂G_z containing (a) 5, (b) 30, (c) 45, (d) 50, (e) 60, (f) 70, (g) 80, and (h) 90 wt% graphene.

Most of the hTS₂₀₀₋₁₂G_z photocatalysts exhibited stable photocatalytic activity between 2 and 4 h; however, to better evaluate the effect of the graphene amount in the composites on the CO and CH₄ production rates, the activities of the composites were examined at the fourth hour (Figure 8a,b). Briefly, with an increase in the graphene content from 0 to 30 wt%, the CO production rate reaches its maximum value (150.5 μmole/g h); this value is 1.56 times greater than that achieved using hTS₂₀₀₋₁₂. This result can be attributed to a reduction in the extent of agglomeration of hTS₂₀₀₋₁₂ with an increase in the graphene content. This same graphene content range has a negligible effect on the CH₄ production rate, while a further increase in the graphene content to 60 wt% results in a dramatic increase in the production of CH₄ but a decrease in the production of CO. Figure 8a,b also shows that the CO production rate is more sensitive to a change in the composite graphene content than the CH₄ production rate. There are three possible reasons for this observation: firstly, it has been reported that the band gap of TiO₂/graphene can decrease with an increase in the graphene content or bond strength between graphene and TiO₂ [31,32]; the bandgap is key when considering product selectivity [5,12,15]. Secondly, improving the degree of dispersion of hTS₂₀₀₋₁₂ on graphene can result in an overall higher catalytic activity potential for the composites. Thirdly, it has been reported that TiO₂ can cause the photodegradation of graphene oxide under irradiation [33], or the formation of Ti-C and Ti-O-C bonds between the C atoms of graphene and Ti atoms in TiO₂ [34], which could lead to changes in the photocatalytic activity of the composite. According to Akhavan et al., the D, G, and 2D bands in the Raman spectrum of graphene oxide change as a function of the irradiation time [33]; this suggests that photodegradation of graphene could also occur for our hTS₂₀₀₋₁₂G_z photocatalysts. This hypothesis was in agreement with the long-term stability test of hTS₂₀₀₋₁₂G₈₀ (Figure S6), which indicates the decay on both CO and CH₄ production rates. In addition, these three factors can influence each other; however, overall, changes in the CO/CH₄ production rates are correlated. Notably, using a graphene mass fraction of 80 wt% in the composite photocatalyst resulted in optimal CO (187.9 μmole/g h; twice that achieved with hTS₂₀₀₋₁₂) and CH₄ (6 times that achieved with hTS₂₀₀₋₁₂) production rates, which could be attributed to the excellent dispersion of hTS₂₀₀₋₁₂ on graphene at this ratio.

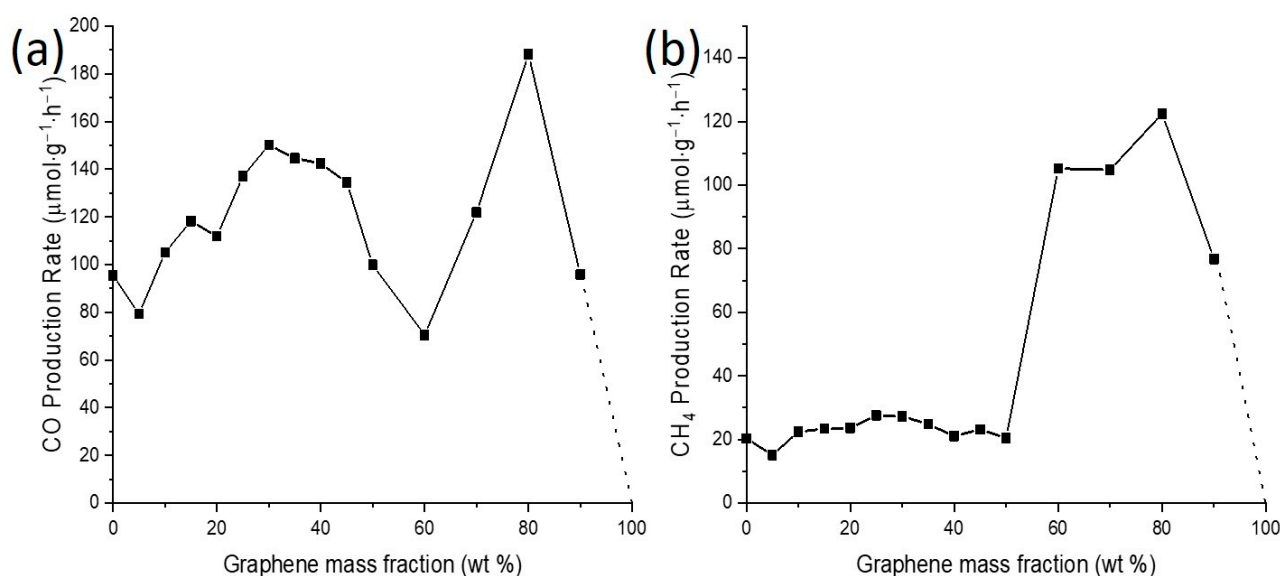


Figure 8. Effect of the graphene mass fraction in hTS_{200-12Gz} on the CO and CH₄ yields achieved through CO₂PR (reaction time: 4 h): (a) CO, and (b) CH₄ yields.

3. Materials and Methods

3.1. Preparation of Silica Microspheres (SS_x)

The silica microspheres (SS_x; x = average diameter) were prepared using a modified version of the procedure reported by Jiang et al., [35]. Briefly, tetraethoxysilane (TEOS; 1.0, 2.4, 5.0, 10.0, or 20.0 mL), the silicon source, was added to a solution containing absolute ethanol (100 mL), deionized water (5, 10, 15, 20, or 30 mL), and ammonia (4.5, 10.0, 15.0, or 20.0 mL) and stirred for approximately 10 min until the liquid became cloudy and white. After stirring for 12 h at room temperature, the suspension was centrifuged (7000 rpm; 10 min), washed with deionized water, and dried. The detailed processing parameters and corresponding specifications of the resultant SS_x are listed in Table S1.

3.2. Preparation of TiO₂/SiO₂ Microspheres (TS_x)

The core-shell SiO₂-TiO₂ microspheres (TS_x) were prepared by a hydrothermal process similar to that reported by Tim et al. [36]. First, SS_x (0.1 g) were suspended in absolute ethanol (100 mL) while stirring vigorously, followed by sonication (30 min) to completely disperse the SS_x. Then, ammonia (0.25 mL) was added dropwise while stirring, followed by the addition of titanium (IV) butoxide (TBT; 0.9 mL) as the titanium source; the mixture was stirred at room temperature for 12 h. The resultant white colloidal spheres were separated by centrifugation (7000 rpm) over 10 min, washed several times with deionized water, and then dried to give the core-shell TS_x microspheres.

3.3. Preparation of Hollow TiO₂ Microspheres (hTS_{x-y})

To remove the silica cores of the hybrid microspheres, 10 mg/mL microsphere suspensions were prepared, shaken in an ultrasonic oscillator for 10 min, and their pH values adjusted to 8, 10, 12, or 14 using 1 M sodium hydroxide and 1 M hydrochloric acid. The solutions were transferred to a Teflon-lined stainless-steel autoclave and heated at 180 °C for 6 h in a programmable oven. The solutions were then centrifuged at 7000 rpm for 10 min, and each separated product washed several times with deionized water, giving the desired hTS_{x-y} (x = average diameter of the cavity, y = processing pH used during the hydrothermal process) after calcination at 470 °C. The detailed processing parameters and corresponding specifications of the resultant hTS_{x-y} materials are listed in Table S2.

3.4. Preparation of the Hollow Titanium Dioxide Microsphere/Graphene Composite Photocatalysts on Quartz Wool ($hTS_{200-12}G_z$)

To further improve the overall photocatalytic activity of hTS_{x-y} , they were modified with commercially available graphene (N002-PDR, Angstrom Materials Inc. (AMI, Taoyuan, Taiwan), as described in the Supplemental Information (Figures S7 and S8)). Briefly, slurries of the photocatalysts, containing designated ratios of hTS_{x-y} /graphene, were prepared in anhydrous ethanol under ultrasonic treatment over 10 min. After drying, the obtained $hTS_{x-y}G_z$ (z = mass fraction of graphene in hTS_{x-y} /graphene) photocatalysts were dispersed on quartz wool. The designated parameters of $hTS_{x-y}G_z$ and the corresponding CO_2PR results are listed in Table 1.

Table 1. Sample designation and corresponding processing parameters.

Designation	Parameter		
	SiO ₂ Microsphere Diameter (x; nm)	Hydrothermal pH Value (y)	Graphene Mass Fraction (z; wt%)
P25 *	–	–	–
$hTS_{x-12}G_0$ *	100, 200, 300, 400	12	0
$hTS_{200-y}G_0$ *	200	8, 10, 12, 14	0
$hTS_{200-12}G_z$ *	200	12	0, 5, 10, 15, 20, 25, 30, 35, 40, 45, 50, 60, 70, 80, 90

* Prepared on a quartz wool substrate.

3.5. Material Characterization

The micro-morphologies and compositions of each photocatalyst were examined by SEM and EDS, respectively, using a JSM-7100F thermal field emission electron microscope. Microscopic structure information was collected using high-resolution TEM (JEOL, Taichung, Taiwan, JEM-1400). Nitrogen adsorption isotherms (77 K) and the Brunauer–Emmett–Teller (BET) method were used to examine the SSAs of the samples (Micromeritics ASAP 2460 volumetric adsorption analyzer, Taichung, Taiwan). The crystalline structures of the TiO₂-related phases were examined by powder XRD using an X'Pert³ powder diffractometer (Cu K α ; λ = 0.15405 nm, Taichung, Taiwan). UV-DRS was performed in the 200–800 nm wavelength range on a dual beam UV-Vis spectrophotometer (DS5, Taichung, Taiwan) equipped with an integrating sphere assembly (BaSO₄ was used as the reflectance standard). FTIR spectra were recorded on a Nicolet™ iS20 (Taichung, Taiwan) spectrometer on powder samples embedded in KBr disks. The photoluminescence (PL) spectra of the samples were obtained using a JASCO FP-8200 (Taichung, Taiwan) fluorescence spectrometer equipped with a 150 W Xe lamp (270 V), using a shielded lamp house as the excitation source.

3.6. Photocatalytic Reaction

The CO_2PR performances of commercial P25 (shown in Figure S9) and the $hTS_{x-y}G_z$ samples were examined using a homemade photoreaction system. Generally, the volume of the reaction chamber was 240 mL with a quartz cover serving as the window for light irradiation from a 100 W Hg lamp. The compositions of the produced gases were analyzed using a gas chromatograph (Agilent 6890 N, Taichung, Taiwan, with He as the carrier gas).

4. Conclusions

In this study, composite photocatalysts composed of hTS and graphene were prepared. The effects of the hTS size, processing pH value, and graphene ratio on the CO_2PR performance of the catalysts were examined. The catalyst cavity size that resulted in the optimal hTS photocatalytic activity was established to be 200 nm (i.e., hTS_{200-y}). Furthermore, the processing pH was found to influence the SSA of the catalyst; the SSAs of the catalysts follow the order: $hTS_{200-12} > hTS_{200-14} > hTS_{200-10} > hTS_{200-8} > p25$. The SiO₂ core was not dissolved at a pH < 12, while pH 14 caused the hTS structure to collapse.

The photocatalyst band gaps are similarly ordered: $\text{hTS}_{200-12} < \text{hTS}_{200-14} < \text{hTS}_{200-10} < \text{hTS}_{200-8}$. The XRD analysis suggested greater lattice strain in hTS_{200-12} than hTS_{200-14} owing to residual SiO_2 in the former; this led to hTS_{200-12} having a smaller band gap and higher photocatalytic activity. As a result, hTS_{200-12} exhibited the best CO_2PR efficiency. Finally, the hTS_{200-12} /graphene ratio used for the composite photocatalysts was studied; a graphene content of 80 wt% resulted in the best hTS_{200-12} dispersion, reducing the extent of agglomeration. As a result, the CO and CH_4 yields obtained via CO_2PR over $\text{hTS}_{200-12}\text{G}_{80}$ were two and six times greater, respectively, than that achieved when using hTS_{100-12} . In short, this study optimized the cavity diameter, processing pH value, and graphene content of hTS /graphene composite photocatalysts, providing a general guideline for the design of hollow microsphere-based photocatalysts for CO_2PR .

Supplementary Materials: The following are available online at <https://www.mdpi.com/article/10.3390/catal11121532/s1>, Table S1: Processing parameters and diameter ranges of silica microspheres. Table S2: Analysis of the Pore Properties of Silica Balls with Different Particle Sizes. Figure S1: XRD patterns of (a) SSx and (b) TSx. Figure S2: FTIR spectra of hTS_{200-y} samples. Figure S3: TEM image of hTS_{x-y} . Figure S4: Long-term stability test of hTS_{200-12} photocatalyst for the production rates of (a) CO and (b) CH_4 . The long-term irradiation was conducted in a commercial photocatalytic system (PCX50BDiscover, PerfectLight) with wavelength of 365 nm, and 50 ml quartz reactor. Figure S5: Effect of CO_2PR reaction time over $\text{hTS}_{200-12}\text{G}_z$ on (a) CO and (b) CH_4 yields. The photoreduction experiments were conducted in a homemade photoreaction system, where the volume of the reaction chamber was 240 mL with a quartz cover serving as the window for light irradiation from a 100 W Hg lamp. Figure S6: Long-term stability test of $\text{hTS}_{200-12}\text{G}_{80}$ photocatalyst for the production rates of (a) CO and (b) CH_4 . Figure S7: (a) SEM and (b) TEM image of graphene. Figure S8: Raman spectrum of N002-PDR graphene powder provided from Angstrom Materials Inc. (AMI). Figure S9: Figure S1 SEM image of P25.

Author Contributions: Y.-C.C. and P.-J.X. partially conducted the experiments and wrote the manuscript. Y.-W.L. initiated the study and conducted sections of the experiments. A.-Y.L. provided experimental resources, and reviewed and edited the manuscript. All authors have read and agreed to the published version of the manuscript.

Funding: This research was funded by the Ministry of Science and Technology (MOST 108-2221-E-167-009-MY3; Taiwan).

Data Availability Statement: Data is contained within the article.

Conflicts of Interest: The authors declare no conflict of interest.

References

- Lo, A.-Y.; Chang, C.-C.; Lai, Y.-W.; Chen, P.-R.; Xu, B.-C. Improving the Supercapacitor Performance by Dispersing SiO_2 Microspheres in Electrodes. *ACS Omega* **2020**, *5*, 11522–11528. [[CrossRef](#)]
- Lo, A.-Y.; Saravanan, L.; Tseng, C.-M.; Wang, F.-K.; Huang, J.-T. Effect of Composition Ratios on the Performance of Graphene/Carbon Nanotube/Manganese Oxide Composites toward Supercapacitor Applications. *ACS Omega* **2020**, *5*, 578–587. [[CrossRef](#)] [[PubMed](#)]
- Lo, A.-Y.; Huang, C.-Y.; Sung, L.-Y.; Louh, R.-F. Low Humidifying Proton Exchange Membrane Fuel Cells with Enhanced Power and Pt-C-h- SiO_2 Anodes Prepared by Electrophoretic Deposition. *ACS Sustain. Chem. Eng.* **2016**, *4*, 1303–1310. [[CrossRef](#)]
- Ran, J.; Jaroniec, M.; Qiao, S.-Z. Cocatalysts in semiconductor-based photocatalytic CO_2 reduction: Achievements, challenges, and opportunities. *Adv. Mater.* **2018**, *30*, 1704649. [[CrossRef](#)]
- Li, X.; Yu, J.; Jaroniec, M.; Chen, X. Cocatalysts for selective photoreduction of CO_2 into solar fuels. *Chem. Rev.* **2019**, *119*, 3962–4179. [[CrossRef](#)] [[PubMed](#)]
- Sohn, Y.; Huang, W.; Taghipour, F. Recent progress and perspectives in the photocatalytic CO_2 reduction of Ti-oxide-based nanomaterials. *Appl. Surf. Sci.* **2017**, *396*, 1696–1711. [[CrossRef](#)]
- Sun, W.; Meng, X.; Xu, C.; Yang, J.; Liang, X.; Dong, Y.; Dong, C.; Ding, Y. Amorphous CoO_x coupled carbon dots as a spongy porous bifunctional catalyst for efficient photocatalytic water oxidation and CO_2 reduction. *Chin. J. Catal.* **2020**, *41*, 1826–1836. [[CrossRef](#)]
- Wang, L.; Zhu, B.; Cheng, B.; Zhang, J.; Zhang, L.; Yu, J. In-situ preparation of TiO_2 /N-doped graphene hollow sphere photocatalyst with enhanced photocatalytic CO_2 reduction performance. *Chin. J. Catal.* **2021**, *42*, 1648–1658. [[CrossRef](#)]

9. Thompson, W.A.; Sanchez Fernandez, E.; Maroto-Valer, M.M. Review and analysis of CO₂ photoreduction kinetics. *ACS Sustain. Chem. Eng.* **2020**, *8*, 4677–4692. [[CrossRef](#)]
10. Liu, J.; Niu, Y.; He, X.; Qi, J.; Li, X. Photocatalytic Reduction of CO₂ Using TiO₂-Graphene Nanocomposites. *J. Nanomater.* **2016**, *2016*, 6012896. [[CrossRef](#)]
11. Fujishima, A.; Honda, K. Electrochemical Photolysis of Water at a Semiconductor Electrode. *Nature* **1972**, *238*, 37–38. [[CrossRef](#)]
12. Lo, A.-Y.; Taghipour, F. Review and prospects of microporous zeolite catalysts for CO₂ photoreduction. *Appl. Mater. Today* **2021**, *23*, 101042. [[CrossRef](#)]
13. Mikrut, P.; Kobieliusz, M.; Macyk, W. Spectroelectrochemical characterization of euhedral anatase TiO₂ crystals—Implications for photoelectrochemical and photocatalytic properties of {001} {100} and {101} facets. *Electrochim. Acta* **2019**, *310*, 256–265. [[CrossRef](#)]
14. Balayeva, N.O.; Mamiyev, Z.; Dillert, R.; Zheng, N.; Bahnemann, D.W. Rh/TiO₂-Photocatalyzed Acceptorless Dehydrogenation of N-Heterocycles upon Visible-Light Illumination. *ACS Catal.* **2020**, *10*, 5542–5553. [[CrossRef](#)]
15. Lo, A.-Y.; Taghipour, F. Ordered Mesoporous Photocatalysts for CO₂ Photoreduction. *J. Mater. Chem. A* **2021**, *9*, 26430–26453. [[CrossRef](#)]
16. Li, Y.; Fu, R.; Gao, M.; Wang, X. B–N co-doped black TiO₂ synthesized via magnesiothermic reduction for enhanced photocatalytic hydrogen production. *Int. J. Hydrogen Energy* **2019**, *44*, 28629–28637. [[CrossRef](#)]
17. Barkhade, T.; Banerjee, I. Optical Properties of Fe doped TiO₂ Nanocomposites Synthesized by Sol-Gel Technique. *Mater. Today: Proc.* **2019**, *18*, 1204–1209. [[CrossRef](#)]
18. Wu, T.; Zhen, C.; Wu, J.; Jia, C.; Haider, M.; Wang, L.; Liu, G.; Cheng, H.-M. Chlorine capped SnO₂ quantum-dots modified TiO₂ electron selective layer to enhance the performance of planar perovskite solar cells. *Sci. Bull.* **2019**, *64*, 547–552. [[CrossRef](#)]
19. Nguyen, C.H.; Tran, M.L.; Tran, T.T.V.; Juang, R.-S. Enhanced removal of various dyes from aqueous solutions by UV and simulated solar photocatalysis over TiO₂/ZnO/rGO composites. *Sep. Purif. Technol.* **2020**, *232*, 115962. [[CrossRef](#)]
20. Diaz-Angulo, J.; Arce-Sarria, A.; Mueses, M.; Hernandez-Ramirez, A.; Machuca-Martinez, F. Analysis of two dye-sensitized methods for improving the sunlight absorption of TiO₂ using CPC photoreactor at pilot scale. *Mater. Sci. Semicond. Process.* **2019**, *103*, 104640. [[CrossRef](#)]
21. Low, J.; Cheng, B.; Yu, J. Surface modification and enhanced photocatalytic CO₂ reduction performance of TiO₂: A review. *Appl. Surf. Sci.* **2017**, *392*, 658–686. [[CrossRef](#)]
22. Tan, L.-L.; Ong, W.-J.; Chai, S.-P.; Goh, B.T.; Mohamed, A.R. Visible-light-active oxygen-rich TiO₂ decorated 2D graphene oxide with enhanced photocatalytic activity toward carbon dioxide reduction. *Appl. Catal. B* **2015**, *179*, 160–170. [[CrossRef](#)]
23. Zhao, H.; Pan, F.; Li, Y. A review on the effects of TiO₂ surface point defects on CO₂ photoreduction with H₂O. *J. Mater.* **2017**, *3*, 17–32. [[CrossRef](#)]
24. Kubacka, A.; Fernández-García, M.; Colón, G. Advanced Nanoarchitectures for Solar Photocatalytic Applications. *Chem. Rev.* **2012**, *112*, 1555–1614. [[CrossRef](#)]
25. Navalón, S.; Dhakshinamoorthy, A.; Álvaro, M.; Garcia, H. Photocatalytic CO₂ Reduction using Non-Titanium Metal Oxides and Sulfides. *ChemSusChem* **2013**, *6*, 562–577. [[CrossRef](#)]
26. Li, K.; An, X.; Park, K.H.; Khraisheh, M.; Tang, J. A critical review of CO₂ photoconversion: Catalysts and reactors. *Catal. Today* **2014**, *224*, 3–12. [[CrossRef](#)]
27. Wang, X.; Xuan, X.; Wang, Y.; Li, X.; Huang, H.; Zhang, X.; Du, X. Nano-Au-modified TiO₂ grown on dendritic porous silica particles for enhanced CO₂ photoreduction. *Microporous Mesoporous Mater.* **2021**, *310*, 110635. [[CrossRef](#)]
28. Wang, T.; Meng, X.; Liu, G.; Chang, K.; Li, P.; Kang, Q.; Liu, L.; Li, M.; Ouyang, S.; Ye, J. In situ synthesis of ordered mesoporous Co-doped TiO₂ and its enhanced photocatalytic activity and selectivity for the reduction of CO₂. *J. Mater. Chem. A* **2015**, *3*, 9491–9501. [[CrossRef](#)]
29. Xue, H.; Wang, T.; Gong, H.; Guo, H.; Fan, X.; Gao, B.; Feng, Y.; Meng, X.; Huang, X.; He, J. Constructing Ordered Three-Dimensional TiO₂ Channels for Enhanced Visible-Light Photocatalytic Performance in CO₂ Conversion Induced by Au Nanoparticles. *Chem. Asian J.* **2018**, *13*, 577–583. [[CrossRef](#)]
30. Tahir, B.; Tahir, M.; Amin, N.A.S. Photocatalytic CO₂ conversion over Au/TiO₂ nanostructures for dynamic production of clean fuels in a monolith photoreactor. *Clean Technol. Environ. Policy* **2016**, *18*, 2147–2160. [[CrossRef](#)]
31. Štengl, V.; Popelková, D.; Vlácil, P. TiO₂-Graphene Nanocomposite as High Performance Photocatalysts. *J. Phys. Chem. C* **2011**, *115*, 25209–25218. [[CrossRef](#)]
32. Lee, J.S.; You, K.H.; Park, C.B. Highly Photoactive, Low Bandgap TiO₂ Nanoparticles Wrapped by Graphene. *Adv. Mater.* **2012**, *24*, 1084–1088. [[CrossRef](#)]
33. Akhavan, O.; Abdolohad, M.; Esfandiar, A.; Mohatashamifar, M. Photodegradation of Graphene Oxide Sheets by TiO₂ Nanoparticles after a Photocatalytic Reduction. *J. Phys. Chem. C* **2010**, *114*, 12955–12959. [[CrossRef](#)]
34. Akhavan, O.; Ghaderi, E. Photocatalytic Reduction of Graphene Oxide Nanosheets on TiO₂ Thin Film for Photoinactivation of Bacteria in Solar Light Irradiation. *J. Phys. Chem. C* **2009**, *113*, 20214–20220. [[CrossRef](#)]
35. Jiang, X.; Tang, X.; Tang, L.; Zhang, B.; Mao, H. Synthesis and formation mechanism of amorphous silica particles via sol-gel process with tetraethylorthosilicate. *Ceram. Int.* **2019**, *45*, 7673–7680. [[CrossRef](#)]
36. Leshuk, T.; Linley, S.; Baxter, G.; Gu, F. Mesoporous Hollow Sphere Titanium Dioxide Photocatalysts through Hydrothermal Silica Etching. *ACS Appl. Mater. Interfaces* **2012**, *4*, 6062–6070. [[CrossRef](#)]